

Highlighting research from Prof. Wei-Ning Wang's group in the Department of Mechanical and Nuclear Engineering at Virginia Commonwealth University, USA.

Facile synthesis of ZnO@ZIF core–shell nanofibers: crystal growth and gas adsorption

ZnO@ZIF core–shell nanofibers were manufactured *via* direct growth of ZIFs on electrospun ZnO nanofibers for the first time. The ZnO@ZIF nanofibers exhibit enhanced CO₂ adsorption performance, mainly due to the large surface area of ZIFs and the unique interaction of CO₂ with the metal sites.

As featured in:



See Wei-Ning Wang *et al.*, *CrystEngComm*, 2017, **19**, 2445.



Cite this: *CrystEngComm*, 2017, **19**, 2445

Received 22nd February 2017,
Accepted 19th April 2017

DOI: 10.1039/c7ce00368d

rsc.li/crystengcomm

ZnO@ZIF-8 core–shell nanofibers were manufactured via direct growth of ZIF-8 on electrospun ZnO nanofibers for the first time. The versatility of this synthesis strategy for other ZnO@ZIF nanofibers was also demonstrated. The as-synthesized ZnO@ZIF-8 nanofibers exhibit enhanced CO₂ adsorption ability and unique adsorption preference as compared to pristine ZnO nanofibers.

In the past several decades, metal organic frameworks (MOFs) have been attracting tremendous attention for various applications, such as gas storage, separation and catalysis,¹ due to their high surface areas, tunable pore sizes and tailorabile surface chemistry.² In addition to pure MOFs, profound attention has also been directed toward the incorporation of MOFs with metals/metal oxides aiming to integrate the functionalities of both materials.^{3,4} These kinds of composites can be produced with several different morphologies, such as films,⁵ hollow spheres,⁶ nanowires⁷ and nanorods.^{8,9} On the other hand, the nanofiber structure is also of great interest, considering its high aspect ratio and ability to avoid aggregation, which is important for many applications, including gas adsorption and catalysis. However, only a few papers have reported the synthesis of metal oxide@MOF composites in the form of nanofibers thus far (e.g., Al₂O₃@MIL-53-NH₂ and TiO₂@UiO-66).^{10–15} The procedures for the fabrication of these metal oxide@MOF nanofibers in the reported papers are similar.^{10–15} In brief, atomic layer deposition (ALD) was employed to deposit metal

oxide layers onto the polymer nanofibers. These metal oxide layers served as the template for the MOFs growth via the solvothermal method. However, the ALD deposition of metal oxide layers involves complicated and multi-step processes, which may limit the further exploration of this strategy.

In order to simplify the synthesis procedure and avoid the use of costly equipment (e.g., ALD), a new strategy was developed in this study for the facile synthesis of metal oxide@MOF nanofibers. Briefly, an electrospinning technique was used to produce polymer nanofibers containing zinc nitrate, which were then calcinated to obtain the zinc oxide (ZnO) nanofibers. These nanofibers subsequently acted as a sacrificial metal source and template for ZIF (zeolitic imidazolate framework) growth to form the ZnO@ZIF core–shell structure. To the best of our knowledge, this is the first demonstration of the facile manufacturing of ZnO@ZIF core–shell nanofibers by using this method. The core–shell

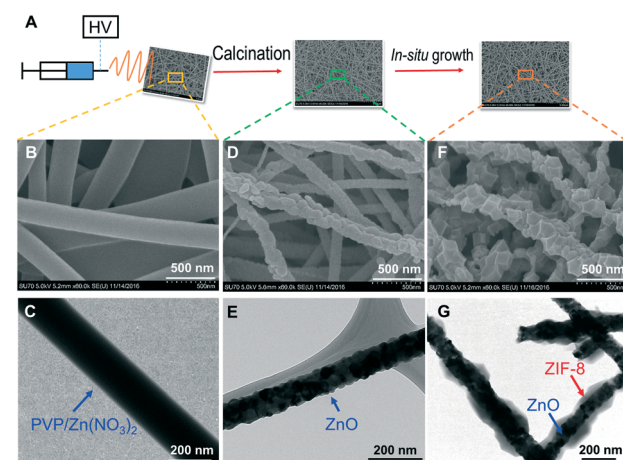


Fig. 1 (A) Schematic illustration of the synthesis procedures; SEM images of (B) electrospun PVP/Zn(NO₃)₂ nanofibers, (D) ZnO nanofibers and (F) ZnO@ZIF-8 nanofibers; TEM images of (C) electrospun PVP/Zn(NO₃)₂ nanofibers, (E) ZnO nanofibers and (G) ZnO@ZIF-8 nanofibers.

^a Department of Mechanical and Nuclear Engineering, Virginia Commonwealth University, Richmond, VA 23219, USA. E-mail: wnwang@vcu.edu; Tel: +1 804 827 4306

^b Department of Chemical and Life Science Engineering, Virginia Commonwealth University, Richmond, VA 23219, USA

† Electronic supplementary information (ESI) available: Synthesis procedure, characterization and DRIFTS analysis, diameter distribution analysis, verification of PVP removal after calcination, transformation of ZnO to ZIF-93, characterization of pure ZIF-8 particles, band gap calculation, size evolution of ZIF-8, BET analysis, supplementary kinetic modelling of CO₂ adsorption, supplementary CO₂ adsorption and desorption and references. See DOI: 10.1039/c7ce00368d

nanofibers combine the functionalities of both ZnO and ZIF. In particular, ZnO has been widely used in gas sensing and catalytic processes.¹⁶ Meanwhile, the ZIF shell, with an excellent gas capture ability, can supply more gas molecules to the ZnO surface, which can help ZnO to achieve better performance.

The synthesis procedures are illustrated in Fig. 1A and detailed in the ESI† (S1). In brief, a mixture of PVP (polyvinylpyrrolidone)/Zn(NO₃)₂·6H₂O/water/ethanol was electrospun to obtain PVP/Zn(NO₃)₂ nanofibers. The as-prepared nanofibers were then calcined at 500 °C in air for 1 hour with a heating rate of 2 °C min⁻¹ to remove PVP and obtain ZnO nanofibers (see S4† for more details). Subsequently, the ZnO nanofibers were immersed in a solution containing 2-methylimidazole (MIM, linker) and *N,N*-dimethylformamide (DMF, solvent), heated at 70 °C for ZIF-8 growth.

As shown in Fig. 1B and C, the PVP/Zn(NO₃)₂ nanofibers exhibit smooth surface and have a geometric mean diameter of 262 nm with narrow diameter distribution with a standard deviation of around 1.2 (Fig. S1A†). After calcination, the PVP was removed and Zn(NO₃)₂ was converted into ZnO as a result of thermal decomposition: 2Zn(NO₃)₂ → 2ZnO + 4NO₂↑ + O₂↑.¹⁷ The surfaces of the ZnO nanofibers turned out to be relatively rough as revealed from the SEM (scanning electron microscopy, Fig. 1D) and TEM (transmission electron microscopy, Fig. 1E) images, where primary ZnO nanocrystals are clearly observed. The size and crystallinity of the ZnO nanocrystals can be controlled by adjusting the calcination temperature and time.¹⁸ Compared with the PVP/Zn(NO₃)₂ nanofibers, the ZnO nanofibers have a smaller geometric mean diameter (144 nm, Fig. S1B†), owing to the removal of PVP and pyrolysis of Zn(NO₃)₂. After immersing the ZnO nanofiber in a 2-methylimidazole ligand solution for 3 hours, ZIF-8 crystals were successfully grown on the surfaces of ZnO nanofibers with rhombic dodecahedron morphology (Fig. 1F and G). The coating of the ZIF-8 shell increased the geometric mean diameter of the nanofiber to 258 nm (Fig. S1C†). The geometric mean diameter of the ZnO core was calculated to be 97 nm (Fig. S1D†) from the TEM images. Based on the changes in diameters of ZnO nanofibers before and after the ZIF growth, the molar ratio of the ZIF-8 shell to the ZnO core was calculated to be 1.2 (see S3† for details). This molar ratio can be tuned by changing the growth conditions for ZIF-8, such as temperature, time, and MIM concentration to achieve optimal performance as needed.

After synthesis, the samples were subjected to detailed characterization. First, X-ray diffraction (XRD) analysis (Fig. 2A) confirms the crystal structures of ZnO and ZIF-8, in line with those reported in literature.^{19,20} Specifically, the diffraction peaks at 31.8°, 34.5° and 36.7° are associated with the (100), (002) and (101) planes of wurtzite hexagonal structure of ZnO crystals (PDF 36-1451), respectively, which is the most thermodynamically stable crystal structure of ZnO at room temperature.²¹ The diffraction peaks at 7.4°, 10.5° and 12.8° correspond to the (011), (002) and (112) planes of ZIF-8 crystals, respectively. In addition to ZIF-8, ZIF-93 was also

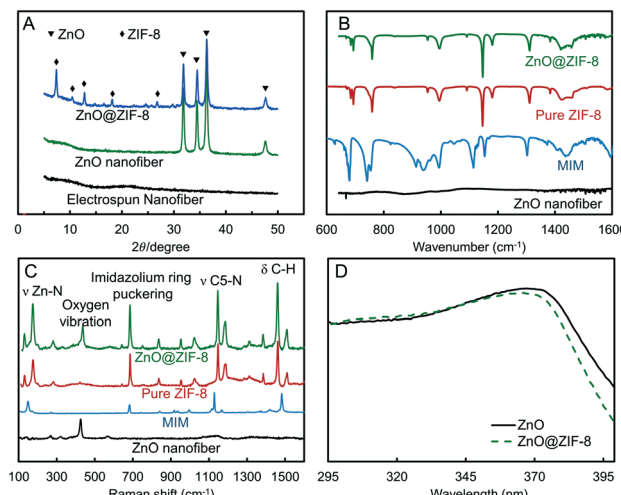


Fig. 2 Characterization of the samples: (A) XRD patterns, (B) FTIR, (C) Raman spectra, and (D) UV-vis spectra.

successfully grown on the ZnO nanofibers (see S5† for details), which demonstrates the versatility of our synthesis method. Interestingly, the growth of ZIF-93 is much slower than ZIF-8. After 3 hour reaction, the XRD peaks of ZIF-93 are still very weak (Fig. S3A†) and only a small amount of metastable ZIF-93 particles are observed in the SEM image (Fig. S3B†). With the extension of reaction time to 24 hours, more regular-shaped ZIF-93 particles are observed (Fig. S3C†) with enhanced characteristic XRD peak intensities at 4.2°, 6.1° and 7.5° (Fig. S3A†). The varying degrees of transformation of ZnO to different ZIFs over the same time period is related to the alkalinity of the ligands. In particular, MIM (ZIF-8 ligand), with a higher alkalinity,²² is expected to have a stronger etching ability than 4-methyl-5-imidazolecarboxaldehyde (4-Me-5-CHOIM, ZIF-93 ligand).

The introduction of surface functional groups was revealed from Fourier transform infrared (FT-IR) analysis. As shown in Fig. 2B, no appreciable peak was observed on the ZnO nanofibers, while intense IR peaks were found for ZnO@ZIF-8 nanofibers, which differ from the MIM's IR peaks but perfectly match with those belonging to pure ZIF-8 particles (see S6† for more characterization results), demonstrating the formation of ZIF-8 crystals on the ZnO nanofibers. Specifically, the observed IR peaks on ZnO@ZIF-8 nanofibers originate from the vibrations of imidazole units, with bending and stretching modes in the spectral region of 600–1350 cm⁻¹ and 1350–1500 cm⁻¹, respectively.^{23,24}

Raman spectroscopy was utilized to understand the vibrational properties of ZnO and ZnO@ZIF-8 nanofibers (Fig. 2C). For ZnO nanofibers, the peak at 436 cm⁻¹ is related to E_{2H} mode, and its strong intensity suggests the long-range crystalline order of ZnO.²⁵ Peaks at 280, 333, 580 cm⁻¹ correspond to B₁^{high}-B₁^{low}, E₂^{high}-E₂^{low}, and E₁(LO) modes, respectively.²⁶ All of the peaks in the Raman spectra for ZnO nanofibers correspond to the various phonon modes of wurtzite ZnO, consistent with the XRD data. The aforementioned

information demonstrates that the obtained ZnO nanofiber is stable and well crystallized. For ZnO@ZIF-8 nanofibers, four new strong peaks appear at 175, 685, 1147, and 1460 cm^{-1} , corresponding to Zn–N stretching, imidazolium ring puckering, C5–N stretching, and C–H bending, respectively.^{27,28} Other small peaks, excluding the ones belonged to ZnO (280, 436 and 580 cm^{-1}), are all associated with the vibrational properties of ZIF-8. The new bands once again confirm the successful growth of ZIF-8 on the ZnO nanofibers.

The UV-vis absorption spectra are displayed in Fig. 2D, demonstrating the variation in the light absorption properties between ZnO@ZIF-8 and ZnO nanofibers, which is attributed to the larger band gap of the core–shell structure (3.241 eV, S7†) as compared that of the pristine ZnO nanofiber (3.229 eV, S7†). This result is consistent with the fact that ZIF-8 (~4.9 eV²⁹) has a much larger band gap than that of ZnO (~3.15 eV³⁰).

Understanding the mechanism and key parameters (*i.e.*, solvent species⁸ and MIM concentration³¹) governing *in situ* ZIF-8 formation on ZnO surface is of significant importance. Initially, 2-methylimidazole acts as an etching reagent to dissolve ZnO and release Zn²⁺ ions, which subsequently coordinate with the MIM ligands to form nuclei and then ZIF-8 crystals.⁸ The ZIF-8 crystals can be generated either in the solution as free particles or *in situ* on the ZnO surface as a shell, determined by the rates of dissolution and coordination.⁸ Specifically, if the dissolution rate is much faster than the coordination rate, the released but uncoordinated Zn²⁺ will diffuse into the solution, thus forming free crystals.³² Several parameters can be adjusted in order to control the dissolution rate, including the solvent species and concentration of MIM. As reported by Zhan *et al.*,⁸ the solvent plays a significant role in determining the Zn²⁺ dissolution rate. As compared to water, DMF has the capability to reduce the etching rate of the ligand and thus the dissolution rate of Zn²⁺. To minimize the possibility of free crystals and assure the formation of a well-defined ZnO@ZIF-8 core–shell structure, pure DMF was used in the current study. In addition to solvent species, MIM concentration also affects the dissolution rate. In particular, high MIM concentration causes rapid Zn²⁺ releasing rate and thus the formation of free ZIF-8 crystals, while low MIM concentration significantly decrease the reaction rate. In this study, an optimized MIM concentration (*i.e.*, 0.08 mol L⁻¹, see S1†) was chosen to ensure the absence of free ZIF-8 crystals while maintaining a reasonable reaction rate.

The growth of ZIF-8 crystals on ZnO nanofibers was monitored with the evolution of morphology (Fig. 3) and crystallinity (Fig. 4) as a function of reaction time. At the initial stage of reaction (*i.e.*, 1 hour), small amount of sphere-like particles appeared on the surface of ZnO nanofibers (Fig. 3A). These particles have a diameter of 74 nm (Fig. S6A†) and poor crystallinity (Fig. 4, black line). Prolonged reaction time (*i.e.* 2 hours and 3 hours) not only increased the crystal size (106 nm after 2 hour reaction, Fig. S6B†) and amount (Fig. 3B and C), but also enhanced the crystallinity (Fig. 4, green and blue line) and

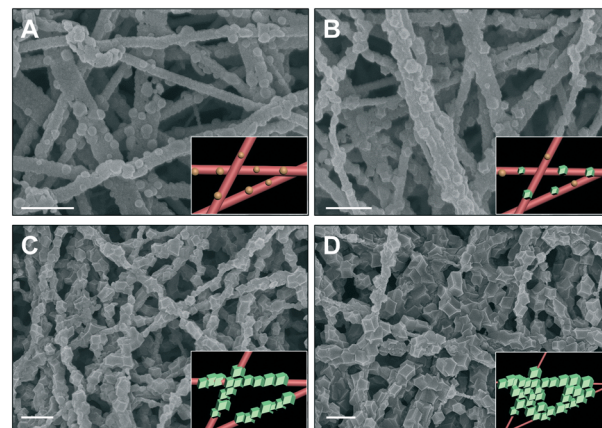


Fig. 3 Time-dependent morphology evolution ZIF-8 on ZnO nanofibers: (A) 1 h, (B) 2 h, (C) 3 h and (D) 6 h. Scale bar: 500 nm.

shapes the particles into rhombic dodecahedron (Fig. 3B and C). As the growth proceeds to 6 hours, the ZIF-8 crystals started to integrate and form a uniform shell (Fig. 3D).

ZIF-8 has been widely used for CO₂ capture.³³ With the incorporation of ZIF-8, the CO₂ uptake of the nanofibers is expected to be improved. Herein, the *in situ* diffuse reflectance infrared Fourier transform spectroscopy (DRIFTS) analysis was conducted in order to assess the CO₂ adsorption capabilities of the core–shell nanofibers. As revealed in Fig. 5A and B, the adsorbed CO₂ gases show two characteristic peaks at 2340 and 2360 cm^{-1} , associated with the antisymmetric stretching modes of CO₂ gas adsorbed on metal sites (Zn²⁺...O=C=O)³⁴ and on functional groups (OH...O=C=O),³⁵ respectively. By comparing the spectra in Fig. 5A and B, higher peaks were observed in the case of ZnO@ZIF-8 nanofibers, intuitively indicating that more CO₂ gases were adsorbed on ZnO@ZIF-8 nanofibers than those on ZnO nanofibers. In addition, the adsorption kinetics were also obtained by recording the IR peak areas as a function of time. As shown in Fig. 5C, ZnO@ZIF-8 core–shell nanofibers show a larger adsorption capacity and faster adsorption rate compared with ZnO nanofibers. CO₂ adsorption experiments

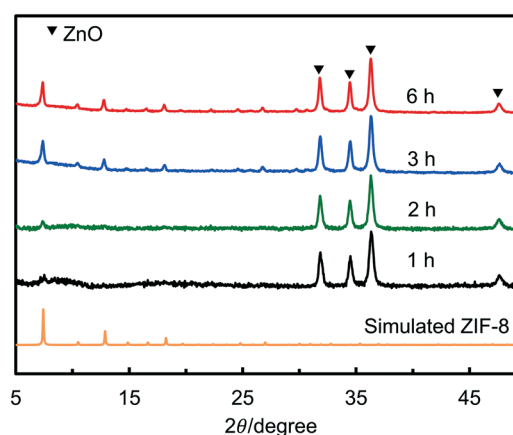


Fig. 4 Time-dependent crystallinity evolution of ZnO@ZIF-8 nanofibers.

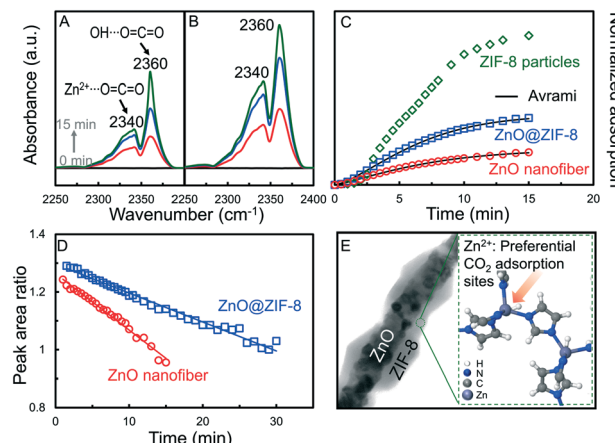


Fig. 5 DRIFTS spectra of adsorbed CO₂: (A) ZnO nanofiber and (B) ZnO@ZIF-8 nanofiber; (C) CO₂ adsorption kinetics; (D) changes of the peak area ratio (Peak₂₃₄₀/Peak₂₃₆₀) as a function of time; (E) illustration of the preferential CO₂ adsorption sites of ZnO@ZIF-8.

were also conducted on the surface of pure ZIF-8 particles. As shown in Fig. 5C, pure ZIF-8 was found to have the best CO₂ adsorption ability. The varying CO₂ adsorption abilities mainly results from the differences in the surface areas. Specifically, pure ZIF-8 has the largest surface area ($1061 \pm 17.7 \text{ m}^2 \text{ g}^{-1}$, S9†), while ZnO nanofibers have the lowest surface area ($20 \pm 1.2 \text{ m}^2 \text{ g}^{-1}$, S9†). With the incorporation of ZIF-8 shell, the surface area of ZnO@ZIF-8 nanofibers is improved to $253 \pm 4.2 \text{ m}^2 \text{ g}^{-1}$ (S9†), but still lower than that of pure ZIF-8, due to the large portion of ZnO in the composite nanofibers. It should be noted that it is desirable to keep ZnO as the core so that its functionalities (e.g., gas sensing and catalytic ability) can be maintained. The ZIF-8 shell is mainly used to capture CO₂ or other gases and supply more gas molecules to the ZnO core for better performance.

The kinetics of CO₂ adsorption on the nanofibers were further simulated by using the least square method with three different models, including pseudo-first order, pseudo-second order and the Avrami model. The equation for each model was listed and detailed in Table 1 and Table S1.† To compare the divergence between the experimental and fitting data, an error function was used as shown below,³⁶

Table 1 Adsorption kinetic constants and error calculated from the fitting of Avrami model

Sample	Avrami model			
	$q_t = q_e(1 - \exp(-(k_A t)^{n_A}))$			
ZnO	0.135	32 687	1.24	2.9
ZnO@ZIF-8	0.144	64 571	1.41	2.2

q_t and q_e (IR peak area per g) are the adsorbed amount at given time (t , min) and equilibrium, respectively; k_A (min⁻¹) is the Avrami kinetic constant; n_A is the Avrami exponent.

$$\text{Error}(\%) = \sqrt{\frac{\sum \left(\frac{q_t(\text{exp}) - q_t(\text{mod})}{q_t(\text{exp})} \right)^2}{N-1}} \times 100 \quad (1)$$

where, $q_t(\text{exp})$ and $q_t(\text{mod})$ are the experimental and modelling adsorbed CO₂ amount (IR peak area per g) at a given time, t (min); N is the number of the data points.

As shown in Table 1 and Table S1,† the Avrami model provides the best fit to the adsorption data with the least error values (<3%). The best fit of the Avrami model to the adsorption data reflects the complexity of CO₂ adsorption on the nanofibers.^{37,38} In addition, a larger Avrami exponent (n_A) was achieved when the ZnO@ZIF-8 core-shell nanofibers were used as the adsorbents, indicating that CO₂ adsorption on the core-shell nanofibers were more contact time dependent.³⁹

In addition to the large surface area of ZIF-8, facilitated interaction of CO₂ with the metal sites in ZIF-8 also contributed to the enhanced CO₂ adsorption on the ZnO@ZIF-8 core-shell nanofibers, which can be evaluated by monitoring the area ratios of Peak₂₃₄₀ to Peak₂₃₆₀. As shown in Fig. 5D, a higher Peak₂₃₄₀/Peak₂₃₆₀ ratio was observed in the case ZnO@ZIF-8 nanofibers, indicating that a larger fraction of CO₂ molecules were adsorbed on metal sites in the presence of ZIF-8, the schematic illustration of which was displayed in Fig. 5E. This preferential interaction of CO₂ with the surface metal sites is caused by the existence of low-coordinated zinc ions at the external surface of ZIF-8. According to the studies of Chizallet and co-workers,^{40,41} due to the crystal cleaving (i.e., linker loss), ZIF-8's external surface is dominated by low-coordinated Zn sites, which act as potential Lewis acid sites and thus facilitate the adsorption of CO₂ molecules. Besides, the interaction of CO₂ with Zn sites could cause greater distortion of CO₂ bond angle and lead to CO₂ bond activation,⁴² which is of great importance for CO₂ photo-conversion process.^{43,44}

In addition, CO₂ desorption experiments were also carried out to assess the reusability of ZnO@ZIF-8 nanofibers. As shown in Fig. S9,† CO₂ can be released from ZnO@ZIF-8 nanofibers under a helium flow (4 mL min⁻¹) at room temperature, indicating good reusability of our samples. In the absence of ZnO (i.e., for pure ZIF-8), similar CO₂ desorption trend was observed. It's worth noting that there was some CO₂ residuals on pure ZIF-8 particles after the same desorption time, which can be attributed to higher CO₂ loading on pure ZIF-8 particles.

Conclusions

A novel strategy was developed to synthesize the ZnO@ZIF core-shell nanofibers. The growth mechanism of ZIF-8 on ZnO nanofibers was explored by monitoring the morphology and crystallinity evolution as a function of reaction time. This core-shell structure has a high CO₂ adsorption ability, mainly due to the large surface area of ZIF-8 and the unique

interaction of CO₂ with the metal sites, and shows great potential for future applications, such as CO₂ photoreduction into hydrocarbon fuels.

Author contributions

W. N. W. designed and supervised the research. X. H. and C. Y. conducted experiments. D. W. performed TEM analysis. S. E. G. helped with BET analysis. D. C. provided insightful discussion on electrospinning. X. H. and W. N. W. wrote the paper. All authors contributed to discussion.

Acknowledgements

The financial supports from Donors of the American Chemical Society (ACS) Petroleum Research Fund (57072-DNI10) and the Virginia Commonwealth University (VCU) Presidential Research Quest Fund are greatly acknowledged. TEM was performed at the VCU Department of Anatomy and Neurobiology Microscopy Facility, with funding from the NIH-NINDS Centre core grant (5P30NS047643). BET measurements were performed in the Catalysis Laboratory funded by the NSF Industry/University Collaborative Research Center grant (IIP1464595).

Notes and references

- N. Stock and S. Biswas, *Chem. Rev.*, 2012, **112**, 933–969.
- O. M. Yaghi, M. O'Keeffe, N. W. Ockwig, H. K. Chae, M. Eddaoudi and J. Kim, *Nature*, 2003, **423**, 705–714.
- G. Lu, S. Li, Z. Guo, O. K. Farha, B. G. Hauser, X. Qi, Y. Wang, X. Wang, S. Han, X. Liu, J. S. DuChene, H. Zhang, Q. Zhang, X. Chen, J. Ma, S. C. J. Loo, W. D. Wei, Y. Yang, J. T. Hupp and F. Huo, *Nat. Chem.*, 2012, **4**, 310–316.
- M.-K. Kim, D. Kim, J. Y. Seo, O. Buyukcakir and A. Coskun, *CrystEngComm*, 2017, DOI: 10.1039/C6CE02549H.
- K. Khaletskaya, S. Turner, M. Tu, S. Wannapaiboon, A. Schneemann, R. Meyer, A. Ludwig, G. Van Tendeloo and R. A. Fischer, *Adv. Funct. Mater.*, 2014, **24**, 4804–4811.
- Y. Liu, W. Zhang, S. Li, C. Cui, J. Wu, H. Chen and F. Huo, *Chem. Mater.*, 2014, **26**, 1119–1125.
- T. Liu, Y. Liu, J. Xu, L. Yao, D. Liu and C. Wang, *RSC Adv.*, 2016, **6**, 91440–91444.
- W.-W. Zhan, Q. Kuang, J.-Z. Zhou, X.-J. Kong, Z.-X. Xie and L.-S. Zheng, *J. Am. Chem. Soc.*, 2013, **135**, 1926–1933.
- W. Zhan, Y. He, J. Guo, L. Chen, X. Kong, H. Zhao, Q. Kuang, Z. Xie and L. Zheng, *Nanoscale*, 2016, **8**, 13181–13185.
- M. Bechelany, M. Drobek, C. Vallicari, A. Abou Chaaya, A. Julbe and P. Miele, *Nanoscale*, 2015, **7**, 5794–5802.
- J. Zhao, D. T. Lee, R. W. Yaga, M. G. Hall, H. F. Barton, I. R. Woodward, C. J. Oldham, H. J. Walls, G. W. Peterson and G. N. Parsons, *Angew. Chem.*, 2016, **128**, 13418–13422.
- J. Zhao, M. D. Losego, P. C. Lemaire, P. S. Williams, B. Gong, S. E. Atanasov, T. M. Blevins, C. J. Oldham, H. J. Walls, S. D. Shepherd, M. A. Browe, G. W. Peterson and G. N. Parsons, *Adv. Mater. Interfaces*, 2014, **1**, 1400040.
- J. Zhao, B. Gong, W. T. Nunn, P. C. Lemaire, E. C. Stevens, F. I. Sidi, P. S. Williams, C. J. Oldham, H. J. Walls, S. D. Shepherd, M. A. Browe, G. W. Peterson, M. D. Losego and G. N. Parsons, *J. Mater. Chem. A*, 2015, **3**, 1458–1464.
- P. C. Lemaire, J. Zhao, P. S. Williams, H. J. Walls, S. D. Shepherd, M. D. Losego, G. W. Peterson and G. N. Parsons, *ACS Appl. Mater. Interfaces*, 2016, **8**, 9514–9522.
- J. Zhao, W. T. Nunn, P. C. Lemaire, Y. Lin, M. D. Dickey, C. J. Oldham, H. J. Walls, G. W. Peterson, M. D. Losego and G. N. Parsons, *J. Am. Chem. Soc.*, 2015, **137**, 13756–13759.
- D. An, Y. Li, X. Lian, Y. Zou and G. Deng, *Colloids Surf., A*, 2014, **447**, 81–87.
- D. Lin, H. Wu, R. Zhang and W. Pan, *Chem. Mater.*, 2009, **21**, 3479–3484.
- A. Senthamizhan, B. Balusamy, Z. Aytac and T. Uyar, *CrystEngComm*, 2016, **18**, 6341–6351.
- S. S. Mali, H. Kim, W. Y. Jang, H. S. Park, P. S. Patil and C. K. Hong, *ACS Sustainable Chem. Eng.*, 2013, **1**, 1207–1213.
- K. S. Park, Z. Ni, A. P. Côté, J. Y. Choi, R. Huang, F. J. Uribe-Romo, H. K. Chae, M. O'Keeffe and O. M. Yaghi, *Proc. Natl. Acad. Sci. U. S. A.*, 2006, **103**, 10186–10191.
- Ü. Özgür, Y. I. Alivov, C. Liu, A. Teke, M. A. Reshchikov, S. Doğan, V. Avrutin, S. J. Cho and H. Morkoç, *J. Appl. Phys.*, 2005, **98**, 041301.
- S. Springer, A. Satalov, J. Lippke and M. Wiebecke, *Microporous Mesoporous Mater.*, 2015, **216**, 161–170.
- Y. Song, D. Hu, F. Liu, S. Chen and L. Wang, *Analyst*, 2015, **140**, 623–629.
- Y. Hu, H. Kazemian, S. Rohani, Y. Huang and Y. Song, *Chem. Commun.*, 2011, **47**, 12694–12696.
- H. Kumar Yadav, R. S. Katiyar and V. Gupta, *Appl. Phys. Lett.*, 2012, **100**, 051906.
- R. Cuscó, E. Alarcón-Lladó, J. Ibáñez, L. Artús, J. Jiménez, B. Wang and M. J. Callahan, *Phys. Rev. B*, 2007, **75**, 165202.
- S. Tanaka, K. Fujita, Y. Miyake, M. Miyamoto, Y. Hasegawa, T. Makino, S. Van der Perre, J. Cousin Saint Remi, T. Van Assche, G. V. Baron and J. F. M. Denayer, *J. Phys. Chem. C*, 2015, **119**, 28430–28439.
- D. Radhakrishnan and C. Narayana, *J. Chem. Phys.*, 2016, **144**, 134704.
- F. Wang, Z.-S. Liu, H. Yang, Y.-X. Tan and J. Zhang, *Angew. Chem., Int. Ed.*, 2011, **50**, 450–453.
- V. Srikant and D. R. Clarke, *J. Appl. Phys.*, 1998, **83**, 5447–5451.
- Q. Yang, W. Liu, B. Wang, W. Zhang, X. Zeng, C. Zhang, Y. Qin, X. Sun, T. Wu, J. Liu, F. Huo and J. Lu, *Nat. Commun.*, 2017, **8**, 14429.
- Y. Sun, Q. Zhang, X. Xu, L. Zhang, Z. Wu, J. Guo and G. Lu, *Eur. J. Inorg. Chem.*, 2016, **2016**, 3553–3558.
- Y. Ban, Z. Li, Y. Li, Y. Peng, H. Jin, W. Jiao, A. Guo, P. Wang, Q. Yang, C. Zhong and W. Yang, *Angew. Chem., Int. Ed.*, 2015, **54**, 15483–15487.
- P. D. C. Dietzel, R. E. Johnsen, H. Fjellvag, S. Bordiga, E. Groppo, S. Chavan and R. Blom, *Chem. Commun.*, 2008, 5125–5127.

- 35 R. Roque-Malherbe, R. Polanco-Estrella and F. Marquez-Linares, *J. Phys. Chem. C*, 2010, **114**, 17773–17787.
- 36 R. Serna-Guerrero and A. Sayari, *Chem. Eng. J.*, 2010, **161**, 182–190.
- 37 A. R. Cestari, E. F. S. Vieira, G. S. Vieira and L. E. Almeida, *J. Hazard. Mater.*, 2006, **138**, 133–141.
- 38 J. Wang, L. A. Stevens, T. C. Drage and J. Wood, *Chem. Eng. Sci.*, 2012, **68**, 424–431.
- 39 S. Chowdhury, G. K. Parshtti and R. Balasubramanian, *Chem. Eng. J.*, 2015, **263**, 374–384.
- 40 C. Chizallet, S. Lazare, D. Bazer-Bachi, F. Bonnier, V. Lecocq, E. Soyer, A.-A. Quoineaud and N. Bats, *J. Am. Chem. Soc.*, 2010, **132**, 12365–12377.
- 41 C. Chizallet and N. Bats, *J. Phys. Chem. Lett.*, 2010, **1**, 349–353.
- 42 H. Wu, J. M. Simmons, G. Srinivas, W. Zhou and T. Yildirim, *J. Phys. Chem. Lett.*, 2010, **1**, 1946–1951.
- 43 K. Teramura, S. Iguchi, Y. Mizuno, T. Shishido and T. Tanaka, *Angew. Chem., Int. Ed.*, 2012, **51**, 8008–8011.
- 44 X. He, Z. Gan, S. Fisenko, D. Wang, H. M. El-Kaderi and W.-N. Wang, *ACS Appl. Mater. Interfaces*, 2017, **9**, 9688–9698.